

# LIRE: LEARNED INVERTIBLE RECONSTRUCTION FOR CONE BEAM CT

NIKITA MORIAKOV, JAN-JAKOB SONKE, AND JONAS TEUWEN

ABSTRACT. Cone Beam CT (CBCT) is a crucial imaging modality in many fields in medicine. However, its potential is not fully utilized due to the generally lower imaging quality than conventional CT, and accurate reconstructions are still a challenging task. Reconstruction methods relying on deep learning have attracted a lot of attention recently due to their promising performance for a variety of medical imaging modalities. There are, however, issues that preclude direct application of such methods to CBCT in practice. Firstly, deep learning reconstruction methods become prohibitively memory expensive when working with fully 3D data such as CBCT. Secondly, deep learning reconstruction methods are widely criticised for being trained and evaluated on data from a specific region of interest such as thorax, raising concerns about generalization to other organs. In this work, we aim to address these shortcomings and propose LIRE: a fully learned, partially invertible primal-dual iterative scheme for Cone Beam CT reconstruction. We drastically reduce memory footprint of the network without sacrificing expressive power by combining reversible residual primal-dual blocks together with patch-wise computations inside the blocks, which allows us to train using clinically-relevant resolutions and projection counts on current consumer hardware. The models are trained on thorax CT scans and tested using both thorax CT and head & neck CT data. We demonstrate that LIRE outperforms the classical methods and the deep learning baseline on both test sets.

arXiv:2205.07358v1 [physics.med-ph] 15 May 2022

## 1. INTRODUCTION

Since its inception in 1960s, Computed Tomography (CT) has enjoyed a huge success in medical imaging. It is characterized by a specific acquisition and reconstruction process, in which a set of X-ray projections is first acquired for varying positions of the source and the detector and where X-rays from the source typically form a narrow fan beam. Subsequently, this projection data is processed by a reconstruction algorithm yielding either a two-dimensional slice or a three-dimensional volume. One of the more recent variants of Computed Tomography is the Cone Beam Computed Tomography (CBCT), where X-rays from the source diverge in a wider cone-shaped beam. Both the source and the detector in CBCT typically follow circular orbits around the isocenter, and the detector is a large flat panel array. CBCT is widely used in clinic nowadays in dentistry [Dawood et al., 2009], interventional radiology [Floridi et al., 2014] and image-guided radiation therapy [Jaffray et al., 2002], in certain cases replacing the classical CT.

CBCT reconstruction, however, is a hard problem. Firstly, it is known [Maaß et al., 2010, Tuy, 1983] that the data completeness condition for exact reconstruction of the whole volume is not satisfied for circular source/detector orbits. CBCT also inherits the imaging artifacts of classical CT such as streaking due to photon starvation in highly attenuated areas, which becomes particularly pronounced for repeated lower dose CBCT scans, and beam hardening. Furthermore, scatter-induced artifacts become more prominent due to the large panel size. These issues result in generally poor Hounsfield unit calibration, which is a serious limitation for applications in radiotherapy, where one would ideally use a daily CBCT scan for treatment plan adjustment without registration to a prior CT scan [Sonke et al., 2019]. This necessitates, along with other applications, the ongoing research on CBCT reconstruction.

In recent years, reconstruction methods based on deep learning have attracted a lot of interest in the community and demonstrated very promising results in public reconstruction challenges. For example, in the recent MRI reconstruction challenges [Muckley et al., 2020, Beauferris et al., 2020] deep learning methods have strongly outperformed the classical baselines. Generally speaking, any medical image reconstruction task can be viewed as an abstract inverse problem for a suitable forward operator, and different approaches have been proposed in the literature for solving such problems with deep learning [Arridge et al., 2019]. We will only consider supervised reconstruction methods in this paper, but we would like to mention that unsupervised methods have also been developed.

One of the possible ways to apply deep learning to CT or CBCT reconstruction problems is to use a neural network as a learned post-processing operator for a classical reconstruction method such as filtered back-projection (FBP). This strategy was investigated in a number of publications, e.g., [Jin et al., 2017], where it has been demonstrated that such learned post-processing can increase the reconstruction quality. At the same time, the neural network in this case does not have direct access to the raw data, thus it can fail to recover from some of the artifacts introduced by the classical reconstruction algorithm.

A rich family of alternative methods is given by *learned iterative schemes*. Such schemes are often inspired by classical iterative schemes, combining the knowledge of the forward operator and its adjoint with neural networks that complement these schemes by e.g. filtering noise in the update term. A particularly important example of such schemes for two-dimensional CT is the Learned Primal-Dual (LPD) algorithm [Adler and Öktem, 2018] which was inspired by the Primal-Dual Hybrid Gradient method [Chambolle and Pock, 2011]. In LPD, computations are performed by *primal blocks* in the image domain and by *dual blocks* in the projection domain, where each block is a small residual convolutional neural network, and the blocks are connected by projection and backprojection operators, enabling end-to-end training. Such architecture allows to filter noise efficiently, since raw projection data is provided to the dual blocks. Extensions of LPD to other modalities have been proposed as well, e.g., DBToR [Teuwen et al., 2021] has shown good results in two-dimensional Digital Breast Tomosynthesis and XPDNet has performed very well on two-dimensional MRI reconstruction in [Ramzi et al., 2020].

Unfortunately, LPD does not scale to a three-dimensional modality such as CBCT due to memory limitations. Indeed, for a  $256 \times 256 \times 256$  float tensor a single convolution layer with 96 features would already require 12 GB memory to perform a backpropagation. This makes it impossible to train LPD on clinically relevant resolutions. Increasing complexity of the primal/dual blocks beyond the simple residual Convolutional Neural Networks would increase memory requirements even further.  $\partial$ U-Net,

which is an alternative, simpler scheme that does not operate in the projection space, was proposed in [Hauptmann et al., 2020], where memory footprint was reduced using a multiscale approach, and reconstructions obtained by primal blocks at different scales are merged together by a U-Net. However, this method still does not allow to train using clinically relevant resolutions, and the expressive power of this scheme is reduced due to the absence of dual blocks and the conservative filter counts that were necessary to reduce memory footprint. As for the unrolled primal-dual schemes like LPD, they have not yet been shown to work in 3D for clinically relevant resolution and projection count, and it is the goal of this work to introduce such a scheme.

## 2. OUR CONTRIBUTION

The key results of this work are:

- We develop LIRE, a practical framework for deep learning-based CBCT reconstruction with clinically-relevant resolution and projection count using a learned iterative scheme that can be trained end-to-end on current consumer GPUs with 24 GB VRAM. Our framework is comprised of a learned primal-dual iterative scheme with residual primal-dual blocks, and a particular set of essential memory optimization techniques that are embedded in the algorithm.
- Two models are trained from scratch for clinical CBCT geometries with small and large field-of-view respectively, where the large field-of-view is accomplished via an offset of the detector panel. We train the models on thorax CT scans with  $256^3$  voxels (2 mm voxel pitch), using a  $256 \times 256$  detector panel (1.6 mm pixel pitch) and either 400 or 720 projections.
- We demonstrate superiority of our method to analytical, iterative and deep learning baselines on the test set of thorax CT scans for both field-of-view settings.
- We demonstrate better out-of-distribution generalization of our method compared to a deep learning baseline for both geometries on a test data set of head & neck CT scans, where our method improves upon analytical and iterative baselines as well.
- We show additionally, as a proof of concept, that using NVIDIA A100 Tensor Core GPUs with 80 GB VRAM our model can be easily fine-tuned on thorax CT scans with  $512^3$  voxels at a native 1 mm voxel pitch,  $512 \times 512$  detector panel and 720 projections. We compare the fine-tuned model with a deep learning baseline, observing superiority of our method.

The major novelties of this work are:

- Our unrolled primal-dual iterative scheme is reversible. To compute the gradients, only the final latent vectors and the sequence of reconstructions returned by the algorithm are needed. This allows to use longer schemes, but on its own does not allow to use complex primal-dual blocks with 3D data due to memory limitations.
- We additionally rely on the local nature of Convolutional Neural Networks (U-net included) and perform patch-wise computations inside the primal-dual blocks during both training and evaluation. During backpropagation, weight gradients received from different patches are summed, giving correct global gradients for network weights.
- Thanks to these novelties, we are able to use 3D U-nets with high filter count inside the primal blocks. Conceptually, our framework allows to use U-nets in both primal and dual blocks, which can be important for scatter correction but also when applying this framework to other modalities such as MRI.
- We provide the network with an auxiliary scalar tensor which has the same shape as the reconstructed volume. In this tensor, intensity of a given voxel contains information about the percentage of projections for which the corresponding spatial location is visible. The network is trained to reconstruct the intensities of all voxels which are visible in at least one projection, which results in a larger field-of-view than FBP.

The minor novelties of this work are:

- Compared to LPD, our scheme maintains a separate variable for the current iteration of reconstruction. The algorithm returns all resulting intermediate reconstructions, the training loss is then computed as the sum of reconstruction losses of these intermediate approximations. This way we aim to benefit from better supervision and also reduce potential gradient vanishing effects. Additionally, the algorithm can be stopped early during inference.

- Compared to LPD, we provide Landweber update term [Kaipio and Somersalo, 2005] to the primal blocks. This update term plays similar role as the gradient of data log-likelihood in Recurrent Inference Machines in [Lønning et al., 2019].

### 3. MATERIALS AND METHODS

**3.1. Tomography and inverse problems.** CBCT reconstruction can be viewed as an inverse problem. Let  $x : z \mapsto x(z)$  be a function specifying the attenuation coefficient for every point  $z \in \Omega_X$  in the spatial domain  $\Omega_X \subset \mathbb{R}^3$ . The circular source rotation orbit is parametrized as a curve  $\gamma : [0, 1] \rightarrow \mathbb{R}^3$ . Detector position and orientation are specified as a family of planes  $\Omega_Y : t \mapsto \Omega_Y(t)$  for  $t \in [0, 1]$ , where each such plane is canonically identified with  $\mathbb{R}^2$ . The line going from the source position  $\gamma(t)$  at time step  $t \in [0, 1]$  to the detector element  $u \in \Omega_Y(t)$  is denoted by  $L_{t,u}$ . The *cone-beam transform operator*, or simply the *projection operator*, is then defined as

$$(1) \quad \mathcal{P}(x)(t, u) = \int_{L_{t,u}} x(z) dz,$$

therefore,  $\mathcal{P}$  is a linear operator mapping functions defined on  $\Omega_X$  to functions defined on  $[0, 1] \times \mathbb{R}^2$ . Hermitian<sup>1</sup> adjoint  $\mathcal{P}^*$  of  $\mathcal{P}$  is called the *backprojection operator*.

Noisy CBCT data acquisition process can then be modeled as

$$(2) \quad y = \text{Poisson}(I_0 \cdot e^{-\mathcal{P}x}),$$

where  $I_0$  is the unattenuated X-ray photon count. The inverse problem of CBCT reconstruction is then to determine the tissue attenuation coefficients  $x$  given the noisy projection data  $y$ .

**3.2. Data.** In this work we simulate two common clinical acquisition geometries for a Linac-integrated CBCT scanner from Elekta [Létourneau et al., 2005]: a small field-of-view setting and a medium field-of-view setting, which will refer to as ‘small FOV setting’ and ‘large FOV setting’. For both settings, the source-isocenter distance is 1000 mm and the isocenter-detector plane distance is 536 mm. For the small FOV setting, the source-isocenter ray passes through the center of the detector, while for the large FOV setting the detector is offset by 115 mm to the side in the direction of rotation. Square detector panel with a side of 409.6 mm and  $256 \times 256$  pixel array was used for the main experiments, while for the additional proof-of-concept study we switched to  $512 \times 512$  pixel array. The projection counts were 400 and 720 for the small FOV and the large FOV setting respectively for the main experiments. The source moves over a 200 degrees arc for the small FOV setting, and for the large FOV setting the source moves over a full circle.

To train and evaluate our models, we collected two diagnostic CT datasets from the institutional archive: a dataset of 424 thorax CT scans with isotropic spacing of 1 mm, and a dataset of 79 head & neck CT scans with anisotropic spacing of between 0.9 mm and 1.0 mm for axial plane and between 1.0 mm and 1.6 mm for the perpendicular direction. Both datasets had axial slice of  $512 \times 512$  voxels. For the main experiments, all data was downsampled by a factor of 2, resulting in volumes with  $256^3$  voxels. For the additional proof-of-concept study, we did not apply any resampling.

The thorax CT dataset was used to train, validate and test the models, while the additional head & neck dataset was used exclusively for testing the models on out-of-distribution data. The thorax CT dataset was partitioned into a training set of 260 scans, a validation set of 22 scans and a test set of 142 scans.

To simulate noisy projection data for the CT scans, Hounsfield units were converted into attenuation coefficients using  $\mu = 0.2 \text{ cm}^{-1}$  as the water linear attenuation coefficient. Attenuated projection data was corrupted by Poisson noise with  $I_0 = 30000$  photons in Eq. (2).

**3.3. Baseline methods.** For the main experiments in this work we considered the following baselines: FBP [Feldkamp et al., 1984], PDHG [Chambolle and Pock, 2011] with TV regularisation and U-net with FBP input.

We used ODL [Adler et al., 2017] implementation of FBP and PDHG. We chose Hann filter with 0.9 frequency modulation for the FBP baseline by testing different combinations of filter and frequency on the training set. Parker weighting was used for FBP reconstruction with small FOV. For FBP reconstruction with large FOV setting it is important to take into account the fact that the central cylindrical region of the volume is measured by twice as many projections as the rest of the FOV,

<sup>1</sup>For suitably defined  $L^2$  function spaces.

this results in a reconstruction artifact in the form of a bright ring around the center of axial volume slices. To reduce this effect, one solution is to smoothly reduce intensity of projections in the detector region which captures twice as much data as we go from the detector center to the detector edge. We do so by multiplying all projections by the following weighting factor [Sen Sharma et al., 2014] after the FBP filtering and before the backprojection:

$$\omega(s) = \begin{cases} 1 & -\Delta \leq s \leq -\Theta \\ \frac{1}{2} \left( -\sin \left( \frac{\pi \arctan(s/D)}{2 \arctan(\Theta/D)} \right) + 1 \right) & -\Theta \leq s \leq \Theta \\ 0 & \Theta \leq s \leq \Delta \end{cases}$$

In this formula,  $s$  is the signed distance between detector a pixel and the projection of the rotation axis onto the detector plane, which is taken with the ‘minus’ sign if we are closer to the detector center than to the edge and with the ‘plus’ sign otherwise,  $D$  is the size of the detector, and  $\Theta = 0.289D$  is a parameter which we chose experimentally for our geometry to obtain uniform reconstructions without the ring artifacts.

For the PDHG baseline, we used 600 iterations with 0.25 weight for the TV regularization term. The parameters of PDHG were obtained via tuning on the train set as well.

Finally, as a main deep learning baseline we implemented a 3D U-net for post-processing the FBP output. We used U-net with 3 downsampling layers, valid convolutions and 64 base filters, similar to [Çiçek et al., 2016], but without Instance or Batch normalization layers. PReLU activation functions were used. As input for the U-net, we provided the FBP reconstruction and the field-of-view tensor  $V_f$  defined later in Section 4.2. Two U-nets, one for small FOV and one for large FOV, were trained for the main experiments on downsampled data using the same augmentation strategy as LIRE and the same loss function as LIRE (see Alg. 2), except for the reconstruction loss over the partial field of view, since FBP quality is very poor in this region. U-nets were trained to reconstruct  $128 \times 128 \times 128$  patches due to memory limitations. Adam optimizer [Kingma and Ba, 2014] was employed with an initial learning rate of 0.0001 and a plateau scheduler with linear warm-up and 10 epoch patience. The best-performing model on the validation set was used for testing. A separate U-net with similar architecture was trained for the proof-of-concept study on high-resolution data; similar to LIRE,  $L^1$  reconstruction loss was minimized in this experiment. One NVIDIA Quadro RTX 8000 was used for training the U-net’s. For the main experiments on downsampled data, it takes U-net+FBP approximately 10 seconds to reconstruct volumes for both geometries. PDHG takes 14 minutes to reconstruct a small FOV volume and 18 minutes to reconstruct a large FOV volume<sup>2</sup>.

Evaluation of LIRE and the baseline methods was performed using PSNR and SSIM metrics restricted to the full field of view region, where  $V_f > 0$ .

## 4. LIRE

**4.1. LIRE architecture and implementation.** LIRE is a data-driven algorithm, where a learned iterative scheme is unrolled and the parameters of this scheme are jointly optimized to minimize expected reconstruction loss over the training dataset. The choice of a particular scheme will, naturally, affect both the performance and the required resources such as GPU memory to train such a scheme.

When designing LIRE, we took inspiration from Learned Primal-Dual (LPD) reconstruction algorithm [Adler and Öktem, 2018]. The main disadvantage of LPD, however, is that it does not scale well to 3D reconstruction problems such as Cone Beam CT. We drastically reduce memory footprint of the LIRE algorithm compared to vanilla LPD and at the same time improve its expressive power by using more complex primal and dual blocks. In order to reduce the memory footprint, we designed LIRE around two main principles: reversibility for network as a whole and patch-wise computations for local operations. We briefly describe these two concepts below. Furthermore, for the additional proof-of-concept experiment on high resolution data, we implemented a CPU-GPU memory streaming mechanism, which would keep entire primal/dual vectors in CPU memory and only send the channels required for computing the primal/dual updates to the GPU.

Reversible residual neural networks were originally introduced in [Gomez et al., 2017]. In a reversible residual network layer, the input tensor  $z$  is split into tensors  $z_1, z_2$  along the channel dimension. The output  $w$  of the layer is then defined by combining  $z_1$  and  $z_2 + \Lambda(z_1)$  back along the channel dimension,

<sup>2</sup>It should be noted that the ODL implementation of PDHG performs a lot of data transfer between CPU and GPU, which hurts the performance.

**Algorithm 1** LIRE.

---

```

1: procedure RECONSTRUCT( $y, \mathcal{P}, \mathcal{P}^*, \theta, V$ )
2:    $x_0 \leftarrow \mathcal{P}^*(y)$  ▷ Normalized backprojection init
3:    $I \leftarrow []$  ▷ Initialize output list
4:    $f \leftarrow x_0^{\otimes 8} \in X^8$  ▷ Initialize primal vector
5:    $h \leftarrow y^{\otimes 8} \in U^8$  ▷ Initialize dual vector
6:   for  $i \leftarrow 1, \dots, 8$  do
7:      $d_1, d_2 \leftarrow \text{SplT}(h)$  ▷ Split dual channels
8:      $p_1, p_2 \leftarrow \text{SplT}(f)$  ▷ Split prime channels
9:      $p_{\text{op}} \leftarrow \mathcal{P}([p_2, x_{i-1}]^{\oplus})$  ▷ Project  $p_2$  and  $x_{i-1}$ 
10:     $d_2 \leftarrow d_2 + \Gamma_{\theta_i^d}([p_{\text{op}}, d_1, y]^{\oplus})$  ▷ Upd.  $d_2$ 
11:     $b_{\text{op}} \leftarrow \mathcal{P}^*(d_2)$  ▷ Backproject  $d_2$ 
12:     $LW \leftarrow \mathcal{P}^*(\mathcal{P}(x_{i-1}) - y)$  ▷ Landweber term
13:     $p_2 \leftarrow p_2 + \Lambda_{\theta_i^p}([b_{\text{op}}, p_1, x_{i-1}, LW, V]^{\oplus})$  ▷ Upd.  $p_2$ 
14:     $h \leftarrow [d_1, d_2]^{\oplus}$  ▷ Combine new dual
15:     $f \leftarrow [p_1, p_2]^{\oplus}$  ▷ Combine new primal
16:     $x_i \leftarrow x_{i-1} + \text{Conv3d}(f, \theta_i^o)$  ▷ Update  $x_{i-1}$ 
17:     $I \leftarrow I + [x_i]$  ▷ Append  $x_i$  to output list
18:     $h \leftarrow \text{Perm}(h, \theta_i^m)$  ▷ Permute dual channels w.  $\theta_i^m$ 
19:     $f \leftarrow \text{Perm}(f, \theta_i^m)$  ▷ Permute prim. channels w.  $\theta_i^m$ 
20:  end for
21:  return  $I$ 
22: end procedure

```

---

**Algorithm 2** Training of LIRE.

---

```

1: procedure LOSS( $x, y, V_f, V_s$ )
2:    $L_1 \leftarrow \|x - y\|_{V_f, 1}$  ▷  $L^1$  loss in full FOV
3:    $L_2 \leftarrow \|x - y\|_{V_s, 1}$  ▷  $L^1$  loss in part. FOV
4:    $S_1 \leftarrow 1.0 - \text{SSIM}_{V_f}(x, y)$  ▷ 1-SSIM, full FOV
5:    $S_2 \leftarrow 1.0 - \text{SSIM}_{V_s}(x, y)$  ▷ 1-SSIM, part. FOV
6:   return  $L_1 + \alpha_1 S_1 + \alpha_2 (L_2 + \alpha_1 S_2)$ 
7: end procedure
8: for  $j \leftarrow 1, \dots, N_{\text{iter}}$  do
9:    $x \sim \mathcal{D}_{\text{train}}$  ▷ Sample train volume
10:   $\Delta \sim \mathcal{N}(0, 100) \in \mathbb{R}^3$  ▷ Sample offset w.r.t. scan center
11:   $\delta \leftarrow x.\text{spacing}$  ▷ Get spacing of volume  $x$ 
12:   $\mathcal{P}, \mathcal{P}^* \leftarrow \mathcal{P}_{\Delta, \delta}, \mathcal{P}_{\Delta, \delta}^*$  ▷ Define projector, backprojector
13:   $\bar{\mathcal{P}}, \bar{\mathcal{P}}^* \leftarrow \mathcal{P}/\|\mathcal{P}\|, \mathcal{P}^*/\|\mathcal{P}^*\|$  ▷ Normalize operators
14:   $y \leftarrow \text{Poisson}(I_0 \cdot e^{-\mathcal{P}(x)})$  ▷ Noisy projections
15:   $\bar{y} \leftarrow -\ln(y)/\|\bar{\mathcal{P}}\|$  ▷ Normalized log-transform
16:   $V_f \leftarrow \text{FullFOV}(\bar{\mathcal{P}})$  ▷ Compute full FOV
17:   $V_p \leftarrow \text{PartialFOV}(\bar{\mathcal{P}})$  ▷ Compute partial FOV
18:   $V_s \leftarrow V_p \setminus V_f$  ▷ Incomplete FOV mask
19:   $I \leftarrow \text{RECONSTRUCT}(\bar{y}, \bar{\mathcal{P}}, \bar{\mathcal{P}}^*, \theta, V_f)$  ▷ Reconstruct
20:   $\text{loss} \leftarrow 0$  ▷ Initialize loss tensor
21:  for  $z \leftarrow I[1], \dots, I[8]$  do ▷ Loop over iterates
22:     $\text{loss} \leftarrow \text{loss} + \text{LOSS}(x, z, V_f, V_s)$  ▷ Increment loss
23:  end for
24:  compute gradients of loss w.r.t.  $\theta$ , update  $\theta$ 
25: end for

```

---

where  $\Lambda$  is a Convolutional Neural Network. Since the input  $z$  can be uniquely restored<sup>3</sup> from the output  $w$ , it is not essential to store intermediate features of  $\Lambda$  prior to the actual computation of gradients for  $\Lambda$ . The main observation behind patch-wise computations is that for neural networks, which are composed solely of local operators such as valid convolutions, activation functions, upsampling and downsampling layers, it is possible to partition the input tensor  $z$  into patches  $z_i, i = 1, \dots, k$  along the spatial dimensions and compute the output patch-by-patch. In general, for every  $i$  it is also necessary to enlarge the patch  $z_i$  by an adding all tensor elements  $\partial z_i \subset z$  within a certain distance to  $z_i$  in order to account for the receptive field of the network when computing features for locations inside  $z_i$ . For a special case of image classification CNNs that do not involve U-net type architectures or non-local operations such a patch-wise computation strategy was used in [Pinckaers et al., 2019].

The reconstruction algorithm is given by the function  $\text{RECONSTRUCT}(y, \mathcal{P}, \mathcal{P}^*, \theta, V)$  in Algorithm 1. Here  $y$  is the log-transformed and scaled projection data,  $\mathcal{P}$  and  $\mathcal{P}^*$  are the normalized projection and backprojection operators respectively,  $\theta$  is a parameter vector and  $V$  is an auxiliary single-channel image space tensor with the same dimensions as the reconstructed volume which we will define later in Section 4.2. Parameters  $\theta$  are partitioned into 4 parameter groups, where  $\{\theta_i^p\}_{i=1}^8$  are the primal block parameters,  $\{\theta_i^d\}_{i=1}^8$  are the dual block parameters,  $\{\theta_i^o\}_{i=1}^8$  are the output convolution parameters and  $\{\theta_i^m\}_{i=1}^8$  are the permutation parameters.

We clarify the notation first. We write  $[z_1, z_2, \dots, z_k]^\oplus$  to denote the channel-wise concatenation of tensors  $z_1, z_2, \dots, z_k$  which are assumed to have the same spatial and batch dimensions. Function  $\text{Split}(z)$  splits tensor  $z$  with  $2n$  channels into tensors  $z_1, z_2$  which get the first  $n$  feature maps of  $z$  and the last  $n$  feature maps of  $z$  respectively. Function  $\text{Perm}(z, \theta_i^m)$  permutes tensor  $z$  with  $n$  channels along the channel dimension with a permutation  $\theta_i^m \in \text{Sym}(n)$ .

In LIRE we use 8 primal/dual iterations (8 primal and 8 dual blocks) with both primal and dual latent vectors having 8 channels. Backprojected data without FBP filtering is used to initialize the reconstruction  $x_0$ . The initial primal vector is defined by stacking 8 copies of  $x_0$ , and the initial dual vector is defined by stacking 8 copies of  $y$ . At the beginning of each iteration  $i = 1, \dots, 8$ , we split the primal and the dual latent vectors along the channel dimension. First we update the dual latent vector in Line 10 of Alg. 1 using dual block  $\Gamma_{\theta_i^d}$  comprised of 3 layers of  $3 \times 3 \times 3$  convolutions with 96, 96 and 4 filters respectively and LeakyReLU activation after the first and the second convolution layer. To update the primal block, we compute the Landweber term in Line 12 of Alg. 1, which plays a similar role as the gradient log-likelihood term in Recurrent Inference Machines in [Lønning et al., 2019]. We update the primal latent vector in Line 13 of Alg. 1 using primal block  $\Lambda_{\theta_i^p}$ . Primal block  $\Lambda_{\theta_i^p}$  is a U-net with a single downsampling layer,  $3 \times 3 \times 3$  valid convolutions with 96 filters in the first double-convolution block, 192 filters in the bottleneck and LeakyReLU activation after all but the last convolution layer. We use average pooling with  $2 \times 2 \times 2$  kernel in the encoder and nearest upsampling in the decoder layer. Primal and the dual updates are computed patch-wise, which is possible thanks to the locality of  $\Gamma_{\theta_i^d}$  and  $\Lambda_{\theta_i^p}$ , during backward pass weight gradients obtained from patches are summed to obtain the global weight gradients. New primal and dual vectors are combined in Lines 14-15. Reconstruction  $x_{i-1}$  is updated in Line 16, where  $\text{Conv3d}$  is a  $1 \times 1 \times 1$  convolution with parameters  $\theta_i^o$ , and we append the new reconstruction  $x_i$  to the output list in Line 17. Finally, we permute the channels of primal and dual latent vectors using the same permutation  $\theta_i^m$  in Lines 18-19. For every  $i$ , the permutation  $\theta_i^m$  is some fixed permutation of  $[1, 2, \dots, 8]$  which is randomly initialized during model initialization and stored as a model parameter; we require that  $\theta_i^m$  mixes the first and the second half of  $[1, 2, \dots, 8]$ .

The algorithm was implemented as a ‘black box’ C++/CUDA extension for PyTorch [Paszke et al., 2019] in order to maximize speed and memory efficiency. Firstly, we implemented the projection and the backprojection operators for CBCT geometry as a CUDA extension for PyTorch. Since both operators are linear and the backprojection operator is the Hermitian adjoint of the projection operator, this is sufficient to enable gradient backpropagation. In the projector code, we followed the same approach as ASTRA Toolbox [van Aarle et al., 2016] and PYRO-NN [Syben et al., 2019] by using texture memory and trilinear interpolation when sampling attenuation values along the source-detector rays. Adjointness of the operators was tested by checking the definition of Hermitian adjoint

$$\langle \mathcal{P}x, y \rangle = \langle x, \mathcal{P}^*y \rangle$$

<sup>3</sup>Up to numerical errors, which are typically negligible in practice for small neural networks.

TABLE 1. Test results on thorax CT and head &amp; neck CT at 2 mm voxel pitch (best result in bold)

Method	Thorax CT		H&N CT		Weight count	Optimizer steps	Batch size
	PSNR	SSIM	PSNR	SSIM			
FBP (small FOV)	15.289	0.572	27.647	0.721	-	-	-
TV (small FOV)	27.370	0.771	33.903	0.866	-	-	-
U-Net (small FOV)	32.405	0.803	36.433	0.879	23341k	284640	1
LIRE (small FOV)	<b>33.345</b>	<b>0.885</b>	<b>37.941</b>	<b>0.971</b>	24497k	6798	8
FBP (large FOV)	20.051	0.662	22.396	0.711	-	-	-
TV (large FOV)	29.237	0.793	37.862	0.945	-	-	-
U-Net (large FOV)	34.297	0.849	37.064	0.885	23341k	287040	1
LIRE (large FOV)	<b>34.432</b>	<b>0.903</b>	<b>40.113</b>	<b>0.982</b>	24497k	6600	8

TABLE 2. Test results on thorax CT at 1 mm voxel pitch (best result in bold)

Method	Thorax CT		Weight count	Optimizer steps	Batch size
	PSNR	SSIM			
U-Net (large FOV)	33.773	0.848	23341k	62400 (cold start)	1
LIRE (large FOV)	<b>35.784</b>	<b>0.881</b>	24497k	1560 (warm start)	2

for random positive test functions (=tensors)  $x, y$ . The LIRE network itself was then built as a C++/CUDA extension for PyTorch by implementing *both* forward and backward passes since automatic differentiation is not available inside C++/CUDA extensions. PyTorch automatic differentiation was still used to compute the gradients of the loss for the output tensors  $x_1, \dots, x_8 \in I$ , but the subsequent computation of the gradients of the parameters  $\theta$  was performed by LIRE in the backward pass. Correctness of the gradient computations for LIRE parameters was verified by computing numerical directional derivatives for random directions inside the parameter space and comparing this with the analytical directional derivatives computed using gradients from LIRE.

**4.2. LIRE training details.** We provide the training procedure for LIRE in Algorithm 2. The training is supervised, and the training set of CT volumes is denoted by  $\mathcal{D}_{\text{train}}$ . We elaborate on the training procedure below.

A CT volume is repeatedly sampled from the training dataset in Line 9 of Alg. 2. During the sampling, augmentations that flip patient left-right and top-bottom are randomly applied, both with probability 50%. We sample a random offset for the rotation center w.r.t. the center of the CT volume from an isotropic Gaussian distribution with 0 mean and a standard deviation of 100 mm in Line 10. Choosing a random offset can be viewed as an additional type of augmentation, furthermore, in practice the isocenter in radiotherapy will be located close to a tumor. We define projection and backprojection operators for the CBCT projection geometry with given volume spacing and center offset in Line 12, and in Line 13 we compute normalized versions of these operators. The operator norm is estimated numerically using power method with three iterations [Boyd, 1974]. Synthetic noisy projection data is computed in Line 14 (see Eq. 2). This noisy projection data is log-transformed and scaled in Line 15. In general, for a realistic CBCT geometry the field of view does not necessarily contain scanned object completely. When comparing reconstruction metrics it is also important to compute these metrics inside an appropriately defined field of view only, since having a large part of the volume set to 0 outside the corresponding field of view would yield over-optimistic reconstruction metrics. We define the full field of view tensor  $V_f$  and the partial field of view tensor  $V_p$  in Lines 16 and 17 respectively, both of these are scalar tensors having same dimensions as the volume that we want to reconstruct. For the projection geometry with small FOV setting, the full field of view tensor is constructed as

$$V_f(p) = \begin{cases} 1 & p \text{ is seen from all projection angles} \\ 0 & \text{otherwise,} \end{cases}$$

while for the projection geometry with large FOV setting the full field of view tensor is constructed as

$$V_f(p) = \begin{cases} 1 & p \text{ is seen from all projection angles} \\ 0.5 & p \text{ is seen from half of the proj. angles} \\ 0 & \text{otherwise.} \end{cases}$$

We chose to use different values (1.0 and 0.5) above to mark the voxels seen from all the projection angles and the voxels which are seen from only half of the angles, however, we expect that the exact numerical values used in these masks are not important. For both small and large field of view settings, the partial field of view is defined as

$$V_p(p) = \begin{cases} 1 & p \text{ is seen from at least one angle} \\ 0 & \text{otherwise.} \end{cases}$$

In particular, this definition of  $V_p$  implies that in the central axial plane all voxels are marked as ‘partially visible’. In Line 18, we define  $V_s$  as the tensor which equals 1 on the set of all voxels  $p$  s.t.  $V_p(p) > 0$ ,  $V_f(p) = 0$  and zero elsewhere. In Line 19, we call the main reconstruction procedure, providing log-transformed normalized projection data, normalized versions of projection and backprojection operators, the collection of weights  $\theta$  and the auxiliary tensor  $V_f$ .  $V_f$  helps the network to deal with the non-homogeneous nature of the reconstruction artifacts.

The reconstruction algorithm returns a list  $I = [z_1, z_2, \dots, z_8]$  of reconstructions, which are obtained after performing 1, 2,  $\dots$ , 8 reconstruction steps respectively. We sum the reconstruction losses over all  $z \in I$  in Line 22. Loss computation takes place in the LOSS function in Alg. 2. We sum losses over the full field of view region, where  $V_f > 0$ , and the partial field of view region, where  $V_s > 0$ . We compute the loss for partial field of view to ensure that the network can provide at least an approximate reconstruction in this region. A linear combination of  $L^1$  loss and Structural Similarity Loss is computed for both regions. We used  $\alpha_1 = 0.1$  for both field of view settings.  $\alpha_2$  was set to 0.1 initially and then reduced to 0.01 after first learning rate decay step.

We trained two versions of LIRE for the main experiments, one for the small FOV setting and one for the large FOV setting. LIRE was trained to reconstruct complete volumes. For the internal patch-based computations inside LIRE we set the patch size to  $128 \times 128 \times 128$ , resulting in roughly 30 GB VRAM usage per single volume. Reducing the patch size to  $32 \times 32 \times 32$  decreased the usage to roughly 20 GB VRAM per single volume. Eight NVIDIA Quadro RTX 8000 GPUs with 48 GB VRAM were used for training LIRE in distributed data parallel mode. We used Adam optimizer [Kingma and Ba, 2014] with an initial learning rate of 0.0001 and a plateau scheduler with linear warm-up and 10 epoch patience. At the end of each epoch models were evaluated, the best model was picked for testing. Training was stopped when we did not observe improvement for more than 15 epochs. For the additional proof-of-concept study on high-resolution data, we performed a warm start from LIRE trained on downsampled lung CT scans with large FOV setting. Two NVIDIA A100 Tensor Core GPUs with 80 GB VRAM inside a virtual machine on NVIDIA TryEGX Platform were used. We employed Adam optimizer with an initial learning rate of 0.000025 and linear warm-up, the model was fine-tuned for 12 epochs without any learning rate decay.  $L^1$  reconstruction loss was used during fine-tuning, due to higher memory costs associated with SSIM loss. LIRE evaluation was performed in the full field of view region, where  $V_f > 0$ , using PSNR and SSIM metrics.

During the inference on the downsampled data with 2 mm voxel pitch and  $256 \times 256$  detector panel, it takes LIRE approximately 104 seconds to reconstruct a single volume on a single Quadro RTX 8000 for the small FOV setting and approximately 115 seconds to reconstruct a volume for the large FOV setting. On high-resolution data with 1 mm voxel pitch,  $512 \times 512$  detector panel and large FOV setting, it takes LIRE approximately 15 minutes to reconstruct a single volume on Quadro RTX 8000, and 6 minutes if A100 is used instead. Faster inference on A100 can be attributed to higher memory bandwidth and other hardware architectural improvements.

## 5. RESULTS

**5.1. Main experiments.** In Table 1 we summarize the results for the test set of thorax CT scans and the out-of-distribution test set of head & neck CT scans. We provide thorax CT axial slices for small FOV in Figure 1, thorax CT coronal slices for small FOV in Figure 2, thorax CT axial slices for large FOV in Figure 3, thorax CT coronal slices for large FOV in Figure 4, head & neck CT axial slices

for large FOV in Figure 5 and head & neck CT coronal slices for large FOV in Figure 6. The slices were taken from randomly chosen test volumes. We see that our method outperforms the classical and deep learning baselines in all cases, including the out-of-distribution test set. Compared to U-net+FBP, most notable is the improvement in SSIM, ranging from +0.05 to +0.08 on thorax CT data, and a much larger field-of-view, since LIRE is not constrained by the data sufficiency region of FBP. PSNR improvement over the U-net is +0.9 dB for small FOV and +0.13 dB for large FOV. On the out-of-distribution test set, we observe better generalization of LIRE compared to U-net+FBP in the form of an increased PSNR and SSIM gap between LIRE and U-net, even though LIRE has a slightly higher parameter count, allowing to suggest that primal-dual schemes with shallow U-nets generalize better than a single deep U-net. Visual inspection of thorax CT slices shows better visibility of lung fissures in LIRE reconstructions compared to the baselines. In head & neck CT slices, we observe that U-net loses spatial resolution and introduces a strong ‘shadow’ in the neck region. LIRE yields best reconstructions on the head & neck CT set due to better handling of photon noise compared to the iterative method, but in the low-noise neck region we observe that the methods are quite close in visual image quality.

Additionally, we measured the performance of LIRE and PDHG on the test set of thorax CT data for the small FOV setting in the region where  $V_f = 0, V_p = 1$ , consisting of the voxels in the partial field of view which do not belong to the full field of view. This way we obtained mean PSNR of 16.938 and mean SSIM of 0.233 for PDHG, whereas for LIRE mean PSNR was 28.156 and mean SSIM was 0.795.

The results of the proof-of-concept high-resolution experiment for the test set of thorax CT scans are summarized in Table 2. We only provide comparison with the U-net+FBP, since it is the best performing baseline method on the downsampled data. We provide high-resolution thorax CT axial slices for large FOV in Figure 7 and high-resolution thorax CT coronal slices for large FOV in Figure 8. In these proof-of-concept experiments, LIRE still outperforms U-net+FBP. Similar to our experiments on downsampled data, visual inspection of the high-resolutions thorax CT slices shows better visibility of lung fissures in LIRE reconstructions compared to the U-net.

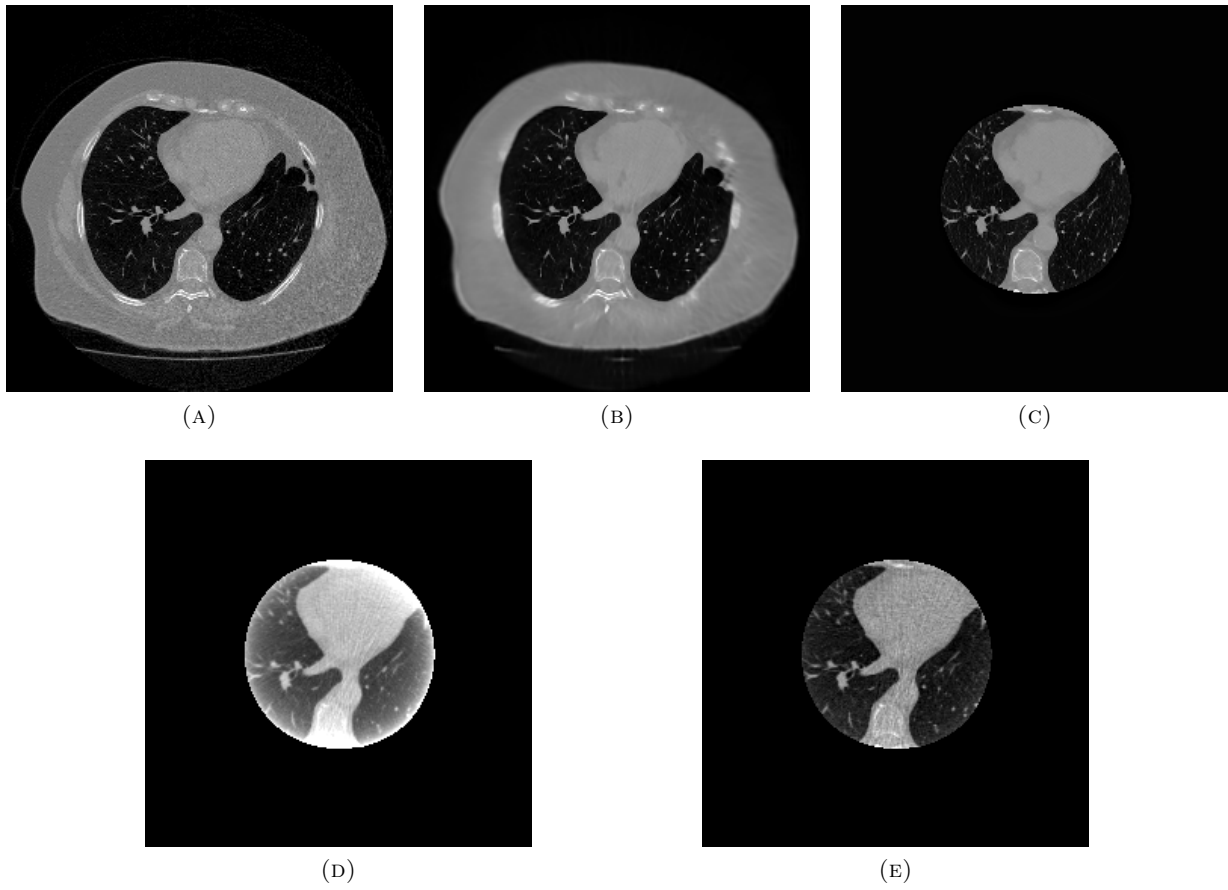


FIGURE 1. (a) Axial slice of Thorax CT with HU range= $(-1000, 800)$ , (b) LIRE/small FOV, (c) U-net/small FOV, (d) FBP/small FOV, and (e) PDHG/small FOV.

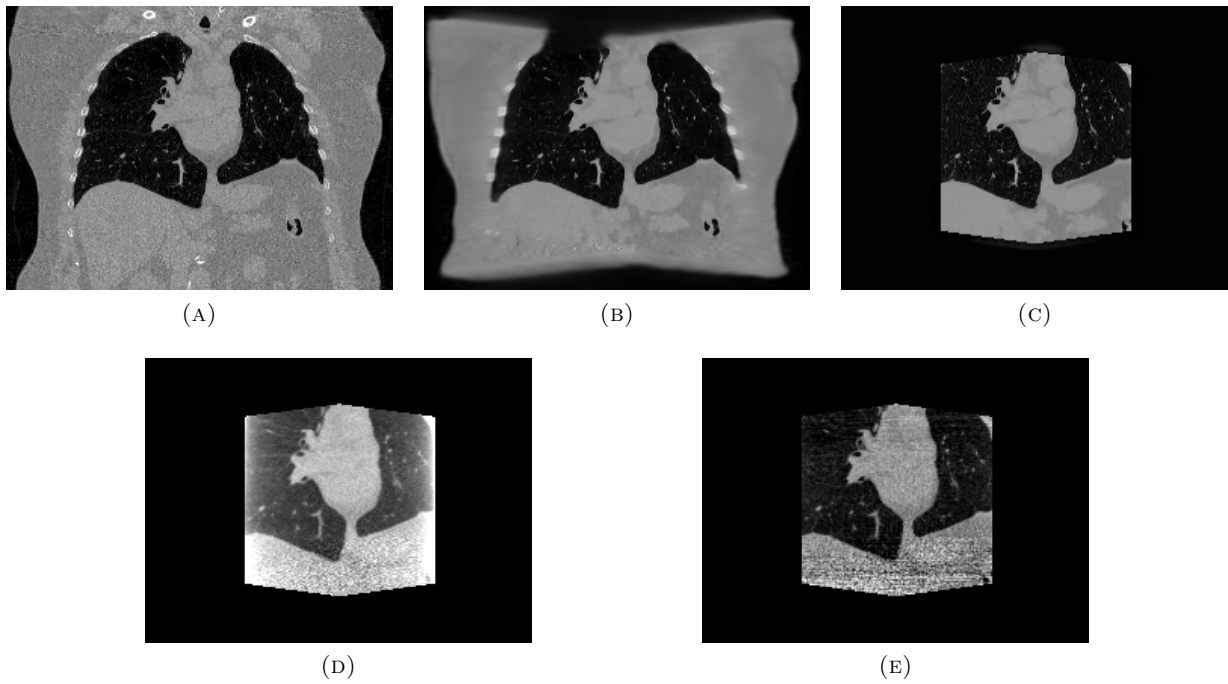


FIGURE 2. (a) Coronal slice of Thorax CT with HU range= $(-1000, 800)$ , (b) LIRE/small FOV, (c) U-net/small FOV, (d) FBP/small FOV, and (e) PDHG/small FOV.

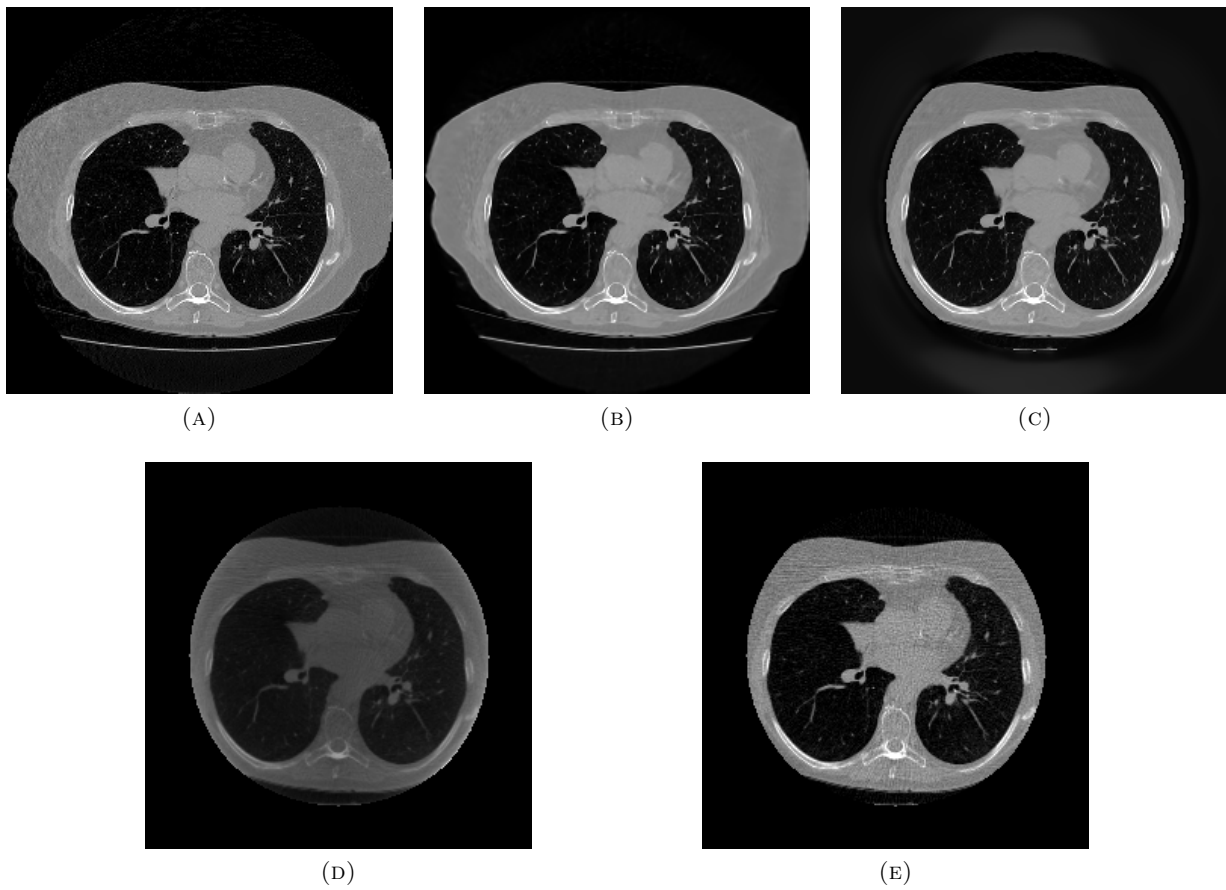


FIGURE 3. (a) Axial slice of Thorax CT with HU range= $(-1000, 800)$ , (b) LIRE/large FOV, (c) U-net/large FOV, (d) FBP/large FOV, and (e) PDHG/large FOV.

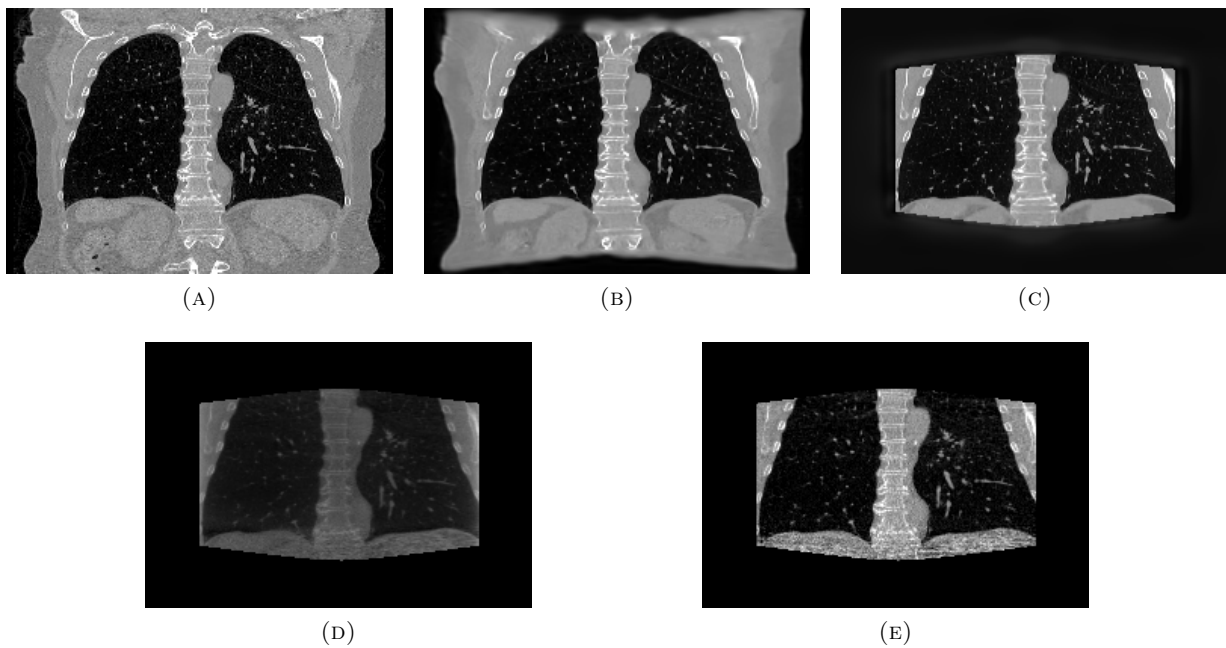


FIGURE 4. (a) Coronal slice of Thorax CT with HU range= $(-1000, 800)$ , (b) LIRE/large FOV, (c) U-net/large FOV, (d) FBP/large FOV, and (e) PDHG/large FOV.

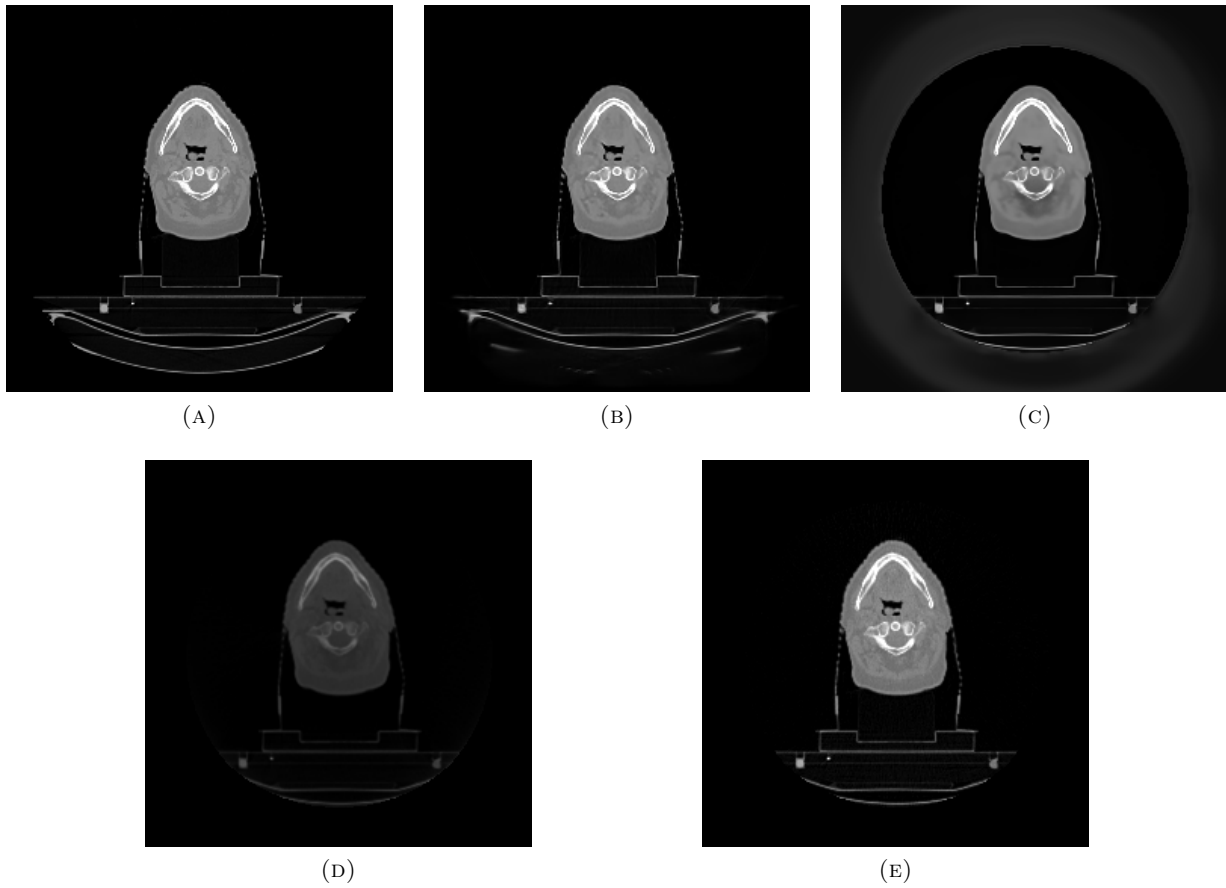


FIGURE 5. (a) Axial slice of Head & Neck CT with HU range= $(-1000, 1000)$ , (b) LIRE/large FOV, (c) U-net/large FOV, (d) FBP/large FOV, and (e) PDHG/large FOV.

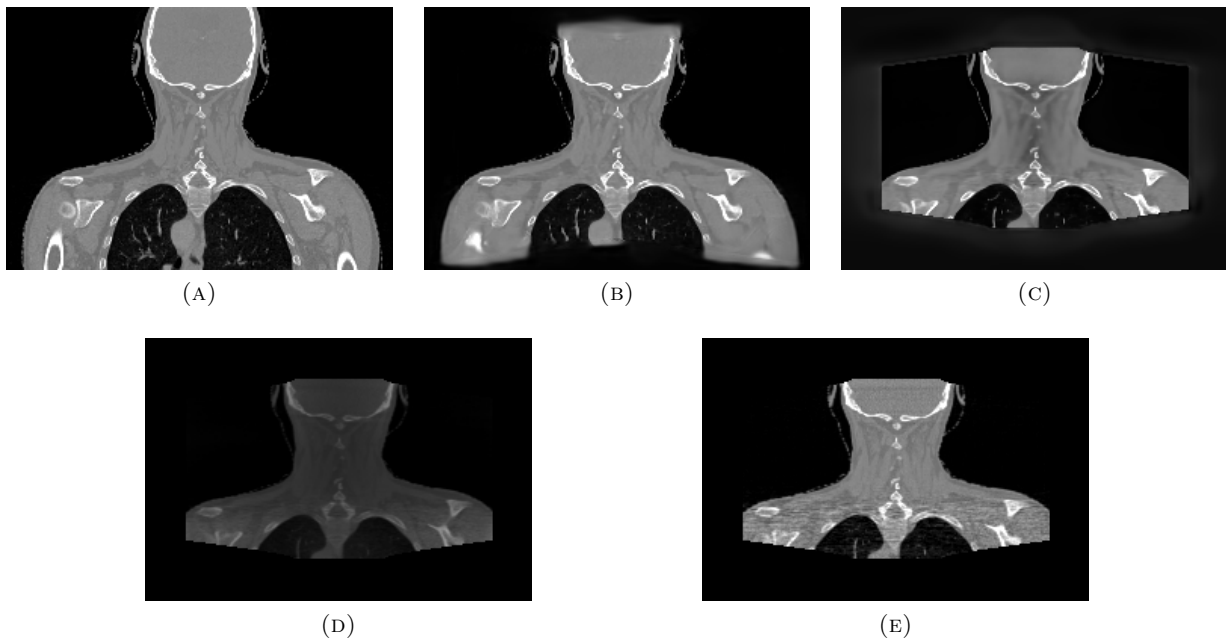


FIGURE 6. (a) Coronal slice of Head & Neck CT with HU range= $(-1000, 1000)$ , (b) LIRE/large FOV, (c) U-net/large FOV, (d) FBP/large FOV, and (e) PDHG/large FOV.

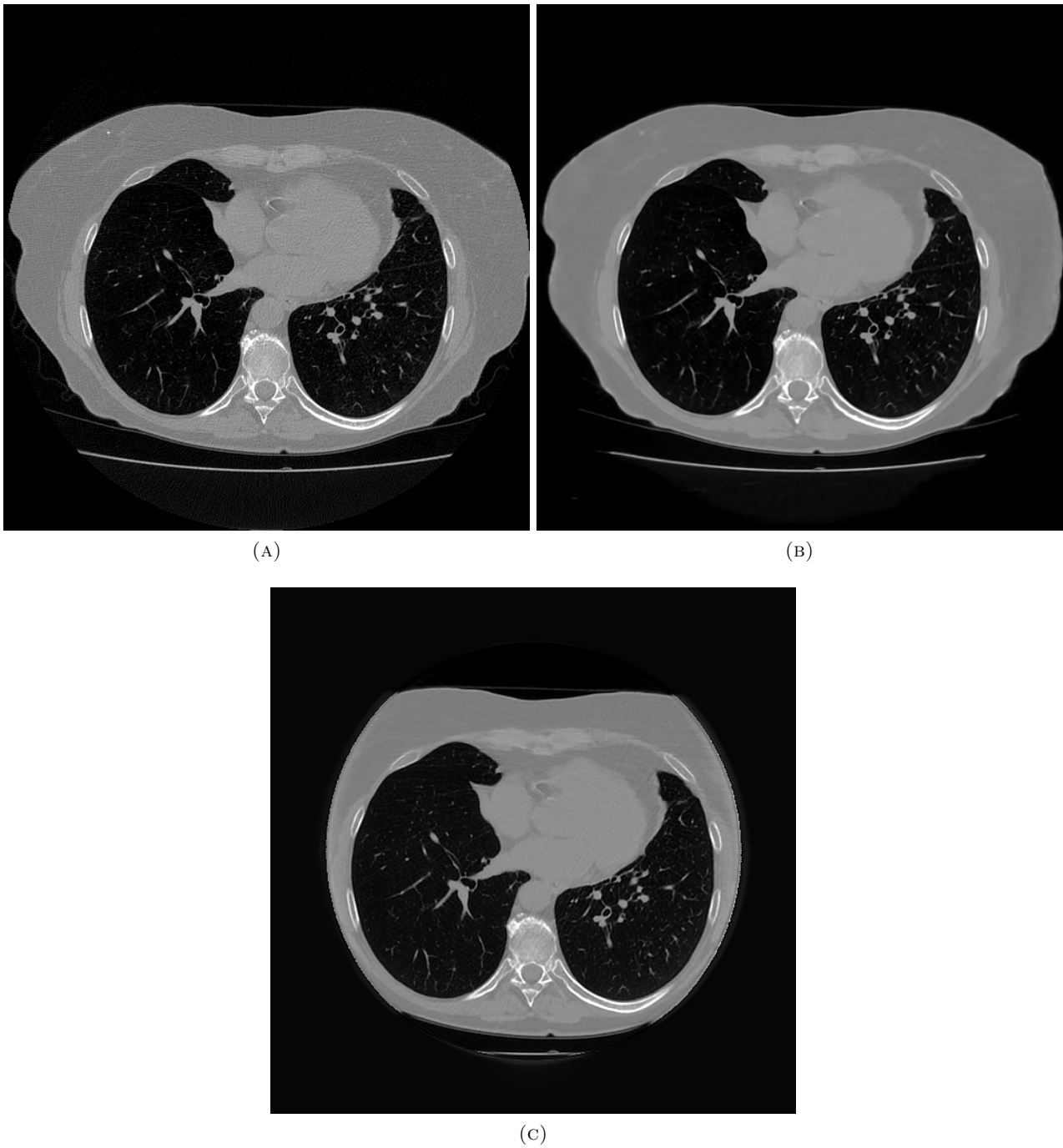


FIGURE 7. (a) High resolution axial slice of Thorax CT with HU range= $(-1000, 800)$ , (b) LIRE/large FOV, (c) U-net/large FOV.

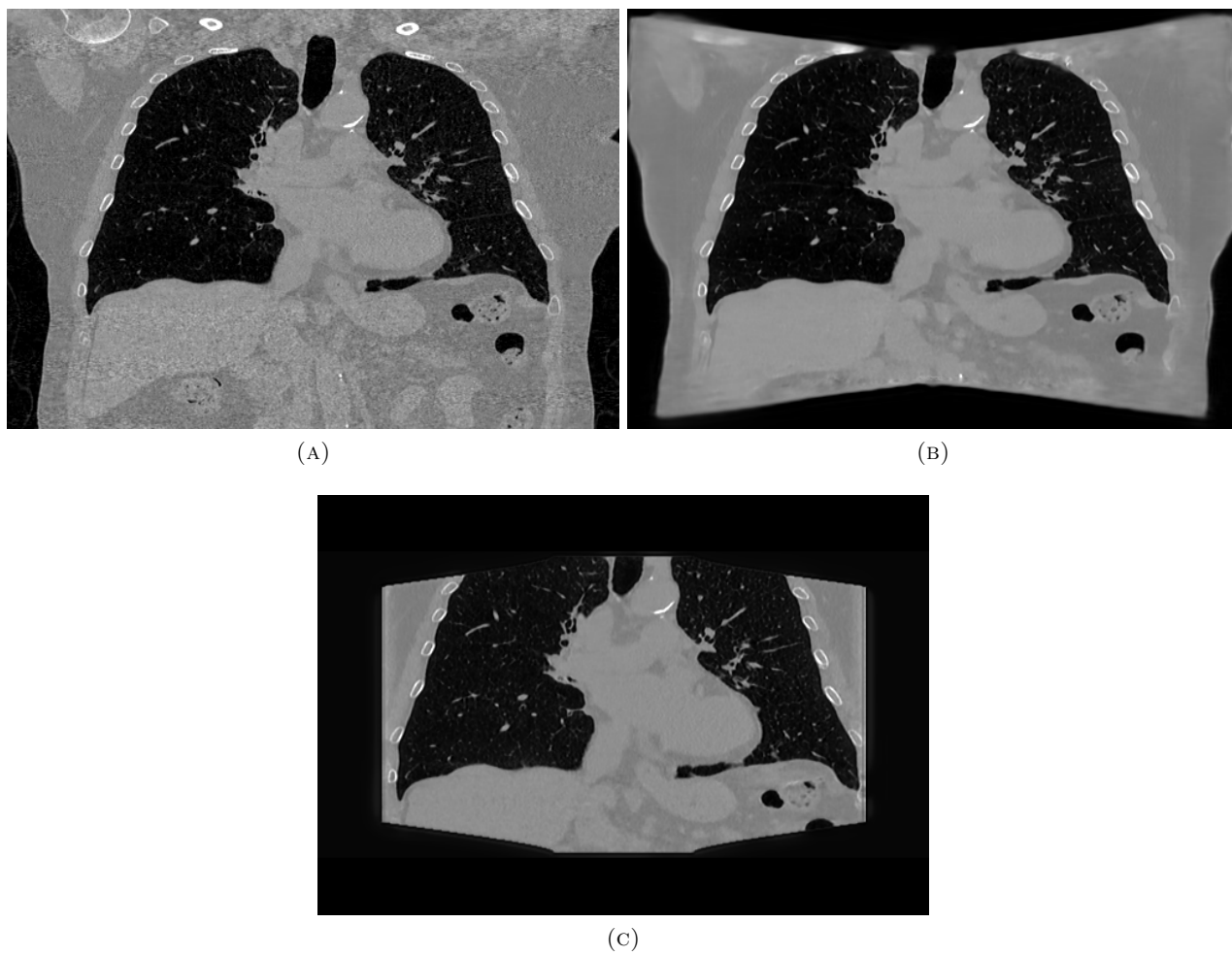


FIGURE 8. (a) High resolution coronal slice of Thorax CT with HU range= $(-1000, 800)$ , (b) LIRE/large FOV, (c) U-net/large FOV.

## 6. DISCUSSION

We have presented LIRE, a practical algorithm for deep learning-based CBCT reconstruction with clinically-relevant resolution and projection count using a learned primal-dual scheme that can be trained end-to-end on current consumer GPUs with 24 GB VRAM. We have shown that our method outperforms the classical and deep learning baselines on the test set of thorax CT scans and the out-of-distribution test set of head & neck CT scans, where we additionally observe better generalization of our method compared to the U-net baseline. In particular, the photon noise in highly attenuated areas is handled very well, which indicates that LIRE can potentially help to lower the dose of CBCT scans. For the small field of view setting, our method is able to reconstruct certain anatomy details outside the full field of view much better than the iterative baseline, which can be interesting for applications in radiotherapy, e.g., by allowing for a better registration of the planning CT scan to the CBCT reconstruction.

This work has certain limitations. Firstly, we do not take scatter artifacts into account. Feasibility of supervised scatter correction with deep learning was demonstrated in e.g. [Maier et al., 2018], and such method can be in principle combined with our learned primal-dual scheme and trained end-to-end. Secondly, we do not correct for possible motion artifacts in thorax CBCT due to breathing or heartbeat. Thirdly, our metrics do not directly imply suitability of our method for radiotherapy planning; a proper Monte Carlo dose simulation would be required to test that.

## 7. ACKNOWLEDGEMENTS

We would like to thank NVIDIA Corporation for providing us with the access to A100 virtual machine instances and for supporting us throughout these experiments. In particular, we would like to thank Joe Cullen from NVIDIA for enabling this collaboration.

## REFERENCES

- J. Adler and O. Öktem. Learned Primal-Dual Reconstruction. *IEEE Transactions on Medical Imaging*, 37(6):1322–1332, jun 2018. ISSN 0278-0062. doi: 10.1109/TMI.2018.2799231.
- J. Adler, H. Kohr, and O. Öktem. Odl 0.6.0, Apr. 2017. URL <https://doi.org/10.5281/zenodo.556409>.
- S. Arridge, P. Maass, O. Öktem, and C.-B. Schönlieb. Solving inverse problems using data-driven models. *Acta Numerica*, 28:1–174, 2019. doi: 10.1017/S0962492919000059.
- Y. Beauferris, J. Teuwen, D. Karkalousos, N. Moriakov, M. Caan, L. Rodrigues, A. Lopes, H. Pedrini, L. Rittner, M. Dannecker, V. Studenyak, F. Gröger, D. Vyas, S. Faghil-Roohi, A. K. Jethi, J. C. Raju, M. Sivaprakasam, W. Loos, R. Frayne, and R. Souza. Multi-channel mr reconstruction (mc-mrrec) challenge – comparing accelerated mr reconstruction models and assessing their generalizability to datasets collected with different coils, 2020.
- D. W. Boyd. The power method for lp norms. *Linear Algebra and its Applications*, 9:95–101, 1974. ISSN 0024-3795. doi: [https://doi.org/10.1016/0024-3795\(74\)90029-9](https://doi.org/10.1016/0024-3795(74)90029-9). URL <https://www.sciencedirect.com/science/article/pii/0024379574900299>.
- A. Chambolle and T. Pock. A first-order primal-dual algorithm for convex problems with applications to imaging. *J. Math. Imaging Vis.*, 40(1):120–145, May 2011. ISSN 0924-9907. doi: 10.1007/s10851-010-0251-1. URL <https://doi.org/10.1007/s10851-010-0251-1>.
- Ö. Çiçek, A. Abdulkadir, S. S. Lienkamp, T. Brox, and O. Ronneberger. 3d u-net: Learning dense volumetric segmentation from sparse annotation. In S. Ourselin, L. Joskowicz, M. R. Sabuncu, G. Unal, and W. Wells, editors, *Medical Image Computing and Computer-Assisted Intervention – MICCAI 2016*, pages 424–432, Cham, 2016. Springer International Publishing. ISBN 978-3-319-46723-8.
- A. Dawood, S. Patel, and J. Brown. Cone beam ct in dental practice. *Br Dent J*, 207:23–28, 2009. doi: <https://doi.org/10.1038/sj.bdj.2009.560>.
- L. A. Feldkamp, L. C. Davis, and J. W. Kress. Practical cone-beam algorithm. *J. Opt. Soc. Am. A*, 1(6):612–619, Jun 1984. doi: 10.1364/JOSAA.1.000612. URL <http://josaa.osa.org/abstract.cfm?URI=josaa-1-6-612>.
- C. Floridi, A. Radaelli, N. Abi-Jaoudeh, M. Grass, M. Lin, M. Chiaradia, J. F. Geschwind, H. Kobeiter, E. Squillaci, G. Maleux, A. Giovagnoni, L. Brunese, B. Wood, G. Carrafiello, and A. Rotondo. C-arm

- cone-beam computed tomography in interventional oncology: technical aspects and clinical applications. *La Radiologia medica*, 119(7):521–532, 2014. doi: <https://doi.org/10.1007/s11547-014-0429-5>.
- A. N. Gomez, M. Ren, R. Urtasun, and R. B. Grosse. The reversible residual network: Backpropagation without storing activations. In I. Guyon, U. V. Luxburg, S. Bengio, H. Wallach, R. Fergus, S. Vishwanathan, and R. Garnett, editors, *Advances in Neural Information Processing Systems*, volume 30. Curran Associates, Inc., 2017.
- A. Hauptmann, J. Adler, S. Arridge, and O. Öktem. Multi-scale learned iterative reconstruction. *IEEE Transactions on Computational Imaging*, 6:843–856, 2020. doi: 10.1109/TCI.2020.2990299.
- D. A. Jaffray, J. H. Siewerdsen, J. W. Wong, and M. A. A. Flat-panel cone-beam computed tomography for image-guided radiation therapy. *Int J Radiat Oncol Biol Phys*, 53(5):1337–1349, 2002. doi: [doi:10.1016/s0360-3016\(02\)02884-5](https://doi.org/10.1016/s0360-3016(02)02884-5).
- K. H. Jin, M. T. McCann, E. Froustey, and M. Unser. Deep convolutional neural network for inverse problems in imaging. *IEEE Transactions on Image Processing*, 26(9):4509–4522, 2017. doi: 10.1109/TIP.2017.2713099.
- J. Kaipio and E. Somersalo. *Statistical and Computational Inverse Problems*, volume 160 of *Applied Mathematical Sciences*. Springer-Verlag, New York, 2005. ISBN 0-387-22073-9. doi: 10.1007/b138659. URL <http://link.springer.com/10.1007/b138659>.
- D. P. Kingma and J. Ba. Adam: A Method for Stochastic Optimization. *arXiv e-prints*, art. [arXiv:1412.6980](https://arxiv.org/abs/1412.6980), Dec. 2014.
- D. Létourneau, J. W. Wong, M. Oldham, M. Gulam, L. Watt, D. A. Jaffray, J. H. Siewerdsen, and A. A. Martinez. Cone-beam-ct guided radiation therapy: technical implementation. *Radiother Oncol*, 75(3):279–286, 2005. doi: [doi:10.1016/j.radonc.2005.03.001](https://doi.org/10.1016/j.radonc.2005.03.001).
- K. Lønning, P. Putzky, J.-J. Sonke, L. Reneman, M. W. Caan, and M. Welling. Recurrent inference machines for reconstructing heterogeneous mri data. *Medical Image Analysis*, 53:64–78, 2019. ISSN 1361-8415. doi: <https://doi.org/10.1016/j.media.2019.01.005>. URL <https://www.sciencedirect.com/science/article/pii/S1361841518306078>.
- C. Maaß, F. Dennerlein, F. Noo, and M. Kachelrieß. Comparing short scan ct reconstruction algorithms regarding cone-beam artifact performance. In *IEEE Nuclear Science Symposium Medical Imaging Conference*, pages 2188–2193, 2010. doi: 10.1109/NSSMIC.2010.5874170.
- J. Maier, Y. Berker, S. Sawall, and M. Kachelrieß. Deep scatter estimation (DSE): feasibility of using a deep convolutional neural network for real-time x-ray scatter prediction in cone-beam CT. In J. Y. Lo, T. G. Schmidt, and G.-H. Chen, editors, *Medical Imaging 2018: Physics of Medical Imaging*, volume 10573, pages 393 – 398. International Society for Optics and Photonics, SPIE, 2018. URL <https://doi.org/10.1117/12.2292919>.
- M. J. Muckley, B. Riemenschneider, A. Radmanesh, S. Kim, G. Jeong, J. Ko, Y. Jun, H. Shin, D. Hwang, M. Mostapha, S. Arberet, D. Nickel, Z. Ramzi, P. Ciuciu, J.-L. Starck, J. Teuwen, D. Karkalousos, C. Zhang, A. Sriram, Z. Huang, N. Yakubova, Y. Lui, and F. Knoll. Results of the 2020 fastMRI Challenge for Machine Learning MR Image Reconstruction. *arXiv e-prints*, art. [arXiv:2012.06318](https://arxiv.org/abs/2012.06318), Dec. 2020.
- A. Paszke, S. Gross, F. Massa, A. Lerer, J. Bradbury, G. Chanan, T. Killeen, Z. Lin, N. Gimelshein, L. Antiga, A. Desmaison, A. Kopf, E. Yang, Z. DeVito, M. Raison, A. Tejani, S. Chilamkurthy, B. Steiner, L. Fang, J. Bai, and S. Chintala. Pytorch: An imperative style, high-performance deep learning library. In H. Wallach, H. Larochelle, A. Beygelzimer, F. d'Alché-Buc, E. Fox, and R. Garnett, editors, *Advances in Neural Information Processing Systems 32*, pages 8024–8035. Curran Associates, Inc., 2019.
- H. Pinckaers, B. van Ginneken, and G. Litjens. Streaming convolutional neural networks for end-to-end learning with multi-megapixel images. *arXiv e-prints*, art. [arXiv:1911.04432](https://arxiv.org/abs/1911.04432), Nov. 2019.
- Z. Ramzi, P. Ciuciu, and J.-L. Starck. Benchmarking MRI Reconstruction Neural Networks on Large Public Datasets. *Applied Sciences*, Mar. 2020. URL <https://hal.archives-ouvertes.fr/hal-03028066>. A short version of this work has been accepted to the 17th International Symposium on Biomedical Imaging (ISBI 2020), April 3-7 2020, Iowa City, IO, USA.
- K. Sen Sharma, H. Gong, O. Ghasemalizadeh, H. Yu, G. Wang, and G. Cao. Interior micro-ct with an offset detector. *Medical Physics*, 41(6), 2014.
- J. J. Sonke, M. Aznar, and C. Rasch. Adaptive radiotherapy for anatomical changes. *Semin Radiat Oncol*, 29(3):245–257, 2019. doi: [doi:10.1016/j.semradonc.2019.02.007](https://doi.org/10.1016/j.semradonc.2019.02.007).

- C. Syben, M. Michen, B. Stimpel, S. Seitz, S. Ploner, and A. K. Maier. Technical Note: PYRO-NN: Python reconstruction operators in neural networks. *Medical Physics*, 46(11):5110–5115, Nov. 2019. doi: 10.1002/mp.13753.
- J. Teuwen, N. Moriakov, C. Fedon, M. Caballo, I. Reiser, P. Bakic, E. García, O. Diaz, K. Michielsen, and I. Sechopoulos. Deep learning reconstruction of digital breast tomosynthesis images for accurate breast density and patient-specific radiation dose estimation. *Medical Image Analysis*, 71:102061, 2021. ISSN 1361-8415. doi: <https://doi.org/10.1016/j.media.2021.102061>. URL <https://www.sciencedirect.com/science/article/pii/S1361841521001079>.
- H. K. Tuy. An inversion formula for cone-beam reconstruction. *SIAM Journal on Applied Mathematics*, 43(3):546–552, 1983. ISSN 00361399. URL <http://www.jstor.org/stable/2101324>.
- W. van Aarle, W. J. Palenstijn, J. Cant, E. Janssens, F. Bleichrodt, A. Dabrovolski, J. D. Beenhouwer, K. J. Batenburg, and J. Sijbers. Fast and flexible x-ray tomography using the astra toolbox. *Opt. Express*, 24(22):25129–25147, Oct 2016. doi: 10.1364/OE.24.025129. URL <http://www.opticsexpress.org/abstract.cfm?URI=oe-24-22-25129>.